

Article

Phosphorus Doping Strategy-Induced Synergistic Modification of Interlayer Structure and Chemical State in $Ti_3C_2T_x$ toward Enhancing Capacitance

Lihong Chen ¹, Yifan Bi ¹, Yunqi Jing ², Jun Dai ³, Zhenjiang Li ¹, Changlong Sun ¹, Alan Meng ⁴, Haijiao Xie ⁵ and Minmin Hu ^{1,*}

¹ School of Materials Science and Engineering, Qingdao University of Science and Technology, Qingdao 266042, China

² College of Environment and Safety Engineering, Qingdao University of Science and Technology, Qingdao 266042, China

³ College of Electromechanical Engineering, Qingdao University of Science and Technology, Qingdao 266061, China

⁴ State Key Laboratory Base of Eco-Chemical Engineering, College of Chemistry and Molecular Engineering, Qingdao University of Science and Technology, Qingdao 266042, China

⁵ Hangzhou Yanqu Information Technology Co., Ltd., Hangzhou 310003, China

* Correspondence: 03581@qust.edu.cn

Abstract: Heteroatom doping is considered an effective method to substantially improve the electrochemical performance of $Ti_3C_2T_x$ MXene for supercapacitors. Herein, a facile and controllable strategy, which combines heat treatment with phosphorous (P) doping by using sodium phosphinate (NaH_2PO_2) as a phosphorus source, is used to modify $Ti_3C_2T_x$. The intercalated ions from NaH_2PO_2 act as “pillars” to expand the interlayer space of MXene, which is conducive to electrolyte ion diffusion. On the other hand, P doping tailors the surface electronic state of MXene, optimizing electronic conductivity and reducing the free energy of H^+ diffusion on the MXene surface. Meanwhile, P sites with lower electronegativity owning good electron donor characteristics are easy to share electrons with H^+ , which is beneficial to charge storage. Moreover, the adopted heat treatment replaces $-F$ terminations with O-containing groups, which enhances the hydrophilicity and provides sufficient active sites. The change in surface functional groups increases the content of high valence-stated Ti with a high electrochemical activity that can accommodate more electrons during discharge. Synergistic modification of interlayer structure and chemical state improves the possibility of $Ti_3C_2T_x$ for accommodating more H^+ ions. Consequently, the modified electrode delivers a specific capacitance of $510 F g^{-1}$ at $2 mV s^{-1}$, and a capacitance retention of 90.2% at $20 A g^{-1}$ after 10,000 cycles. The work provides a coordinated strategy for the rational design of high-capacitance $Ti_3C_2T_x$ MXene electrodes.

Keywords: MXene; supercapacitor; energy storage; pseudocapacitance; P doping



Citation: Chen, L.; Bi, Y.; Jing, Y.; Dai, J.; Li, Z.; Sun, C.; Meng, A.; Xie, H.; Hu, M. Phosphorus Doping Strategy-Induced Synergistic Modification of Interlayer Structure and Chemical State in $Ti_3C_2T_x$ toward Enhancing Capacitance. *Molecules* **2023**, *28*, 4892. <https://doi.org/10.3390/molecules28134892>

Academic Editors: Jin Jia and Yucheng Lan

Received: 24 May 2023

Revised: 14 June 2023

Accepted: 15 June 2023

Published: 21 June 2023



Copyright: © 2023 by the authors. Licensee MDPI, Basel, Switzerland. This article is an open access article distributed under the terms and conditions of the Creative Commons Attribution (CC BY) license (<https://creativecommons.org/licenses/by/4.0/>).

1. Introduction

Electrochemical energy storage devices are considered one of the most promising energy storage technologies to solve the global energy crisis, with batteries and supercapacitors as the two main devices [1,2]. In particular, supercapacitors have significant advantages such as high specific energy, high power density, long cycle life, and rapid charging and discharge [3–5], which can be classified into electrical double layer capacitors (EDLCs) and pseudocapacitors (PCs) [6]. EDLCs tend to exhibit lower energy density due to the limited accessible surface area, instead, PCs can store more charges by their Faradaic redox mechanism [7,8]. However, most well-studied pseudocapacitive materials, such as conducting polymers and transition metal oxides, suffer from volumetric swelling/contraction, limited cycling performance, and high electrode resistance [9,10].

Thus, the exploration of new electrode materials with outstanding electrochemical performance is an imminent challenge for developing high-performance energy storage devices.

MXene, a family of two-dimensional (2D) transition metal carbide/nitride, has attracted great attention as a pseudocapacitive electrode material in electrochemical energy storage due to its good conductivity, excellent hydrophilicity, large specific surface area, high mechanical strength, and adjustable interlayer spacing [11–17]. The most promising type of MXene, $\text{Ti}_3\text{C}_2\text{T}_x$, is obtained by etching Al layers in the Ti_3AlC_2 MAX phase with HF [18–20], HCl–LiF [21], or Lewis acidic molten salt [22], where T represents terminal groups –O, –OH, or –F on the surface of $\text{Ti}_3\text{C}_2\text{T}_x$, and x is the number of terminal groups [23,24]. In H_2SO_4 electrolyte, $\text{Ti}_3\text{C}_2\text{T}_x$ has a high theoretical capacitance due to the efficient electric double layer (EDL) charge accumulation in the interlayer space and the fast pseudocapacitive proton insertion/desertion by surface redox reactions [25].

Generally, the capacitive performance of MXene is primarily determined by its surface chemistry state, which dictates the interaction mechanism and binding strength between the adsorbates and MXenes and thus contributes to the electrochemical performance [26]. Among the terminations of MXene (–O, –OH, –F), –O groups with lower electronegativity (3.5) own good electron donor characteristics, which not only facilitates the electrostatic accumulation of electrons at the electrode surface, giving rise to the increase in EDL capacitance but also works as active sites for proton bonding/debonding, leading to the enhancement in pseudocapacitance. Moreover, when MXene is doped with heteroatom N with lower electronegativity (3.04), a significant improvement in electrochemical performance is achieved by structural, compositional, and surface electronic regulation. For example, Yang et al. prepared nitrogen-doped $\text{Ti}_3\text{C}_2\text{T}_x$ by annealing in ammonia, which yields 192 F g^{-1} at 1 mV s^{-1} in $1 \text{ M H}_2\text{SO}_4$ and remains 67% of initial capacitance over the scan rates from 1 to 200 mV s^{-1} [27]. Zhang et al. prepared a nitrogen-doped $\text{Ti}_3\text{C}_2\text{T}_x$ film electrode with a hydrothermal method using hydrazine hydrate as a nitrogen source, which delivers 340 F g^{-1} at 2 mV s^{-1} and no capacitance degradation after 10,000 cycles in $1 \text{ M H}_2\text{SO}_4$ [28]. Pu et al. prepared a new type of N-doped MXene electrode from non-toxic biological chitosan, which delivers 286.28 F g^{-1} and maintains almost 100% retention after 10,000 cycles [29]. Therefore, we believe that introducing phosphorus heteroatom with lower electronegativity (2.19) can develop a higher capacitance MXene electrode by trimming the electron donor capability, and modifying the surface electrical and chemical properties. In addition, P heteroatom doping is considered an effective and convenient modification strategy to improve the electrochemical performance of carbon materials [30,31]. Although there are several reported works in regard to P doping MXene in supercapacitors, the doping effect is not ideal and the underlying doping mechanism, especially the doping positions/configurations, and their effect on capacitance enhancement are still unexplored.

Inspired by the above motivation, in this work, a phosphorus doping strategy (high-temperature heat treatment with NaH_2PO_2 as the phosphorus source) was employed to obtain the electrode material of supercapacitor (P– $\text{Ti}_3\text{C}_2\text{T}_x$) with high specific capacitance and excellent cyclic performance. Morphology and component characterization, DFT calculation, and electrochemical kinetic analysis have been used to give deep insight into the mechanism of improvement in electrochemical performance. As revealed, P doping improved electrical conductivity and reduced the free energy of H^+ diffusion on the MXene surface. Meanwhile, the intercalated ions acted as “pillars” to expand the interlayer space of MXene, which is conducive to electrolyte ion diffusion. Moreover, the adopted high-temperature heat treatment in the P doping strategy replaced –F terminations with O-containing groups, which enhances the hydrophilicity and provides sufficient electrochemical active sites for H^+ . Synergistic modification of interlayer structure and chemical state improves the possibility of $\text{Ti}_3\text{C}_2\text{T}_x$ for accommodating more H^+ ions, further enhancing the capacitance of $\text{Ti}_3\text{C}_2\text{T}_x$.

2. Results and Discussion

2.1. Materials Characterization

The morphologies and microstructures of the prepared samples were analyzed by using scanning electron microscopy (SEM) and transmission electron microscopy (TEM). $\text{Ti}_3\text{C}_2\text{T}_x$ and $\text{P-Ti}_3\text{C}_2\text{T}_x$ display the same structure with an accordion shape (Figure 1a,b), proving that the surface morphology of $\text{Ti}_3\text{C}_2\text{T}_x$ is not affected after annealing treatment with $\text{NaH}_2\text{PO}_2 \cdot \text{H}_2\text{O}$. The smooth and thin $\text{P-Ti}_3\text{C}_2\text{T}_x$ nanosheets are observed in the TEM image (Figure 1c), further indicating the maintenance of a lamellar structure. Moreover, a high-resolution transmittance electron microscopy (HRTEM) image of $\text{P-Ti}_3\text{C}_2\text{T}_x$ (Figure 1c insert) shows a hexagonal structure demonstrated by different grain orientations with 60° angles and lattice fringes of 0.26 nm which is attributed to the (100) lattice planes of the $\text{Ti}_3\text{C}_2\text{T}_x$. Fourier transform infrared (FTIR) spectra were used to investigate the change in the surface chemical state of $\text{Ti}_3\text{C}_2\text{T}_x$ upon P doping (Figure 1d), which indicates the presence of several common peaks belonging to $\text{Ti}_3\text{C}_2\text{T}_x$ MXene, such as Ti-C ($\sim 555 \text{ cm}^{-1}$), Ti-F ($\sim 800 \text{ cm}^{-1}$), C-O/C=O ($\sim 1640 \text{ cm}^{-1}$) and -OH ($\sim 3440 \text{ cm}^{-1}$) in the range of $400\text{--}4000 \text{ cm}^{-1}$ [32–34]. Notably, the new peak in $\text{P-Ti}_3\text{C}_2\text{T}_x$ appearing near 1120 cm^{-1} corresponds to the P-O bond, which suggests that P atoms are successfully doped in $\text{Ti}_3\text{C}_2\text{T}_x$ [26]. In addition, the energy dispersive spectroscopy (EDS) spectrum and element mapping images display the presence and uniform distribution of Ti, C, O, and P elements in $\text{P-Ti}_3\text{C}_2\text{T}_x$ (Figure 1e,f), testifying that P atoms are successfully doped, which match well with the result of FTIR analysis.

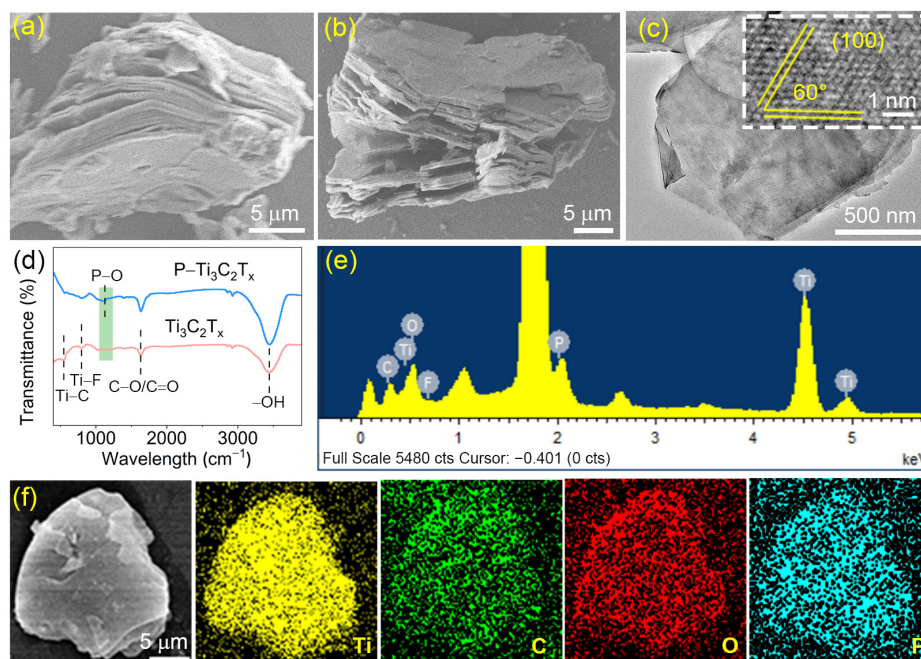


Figure 1. Morphology and structure characterization of $\text{Ti}_3\text{C}_2\text{T}_x$ and $\text{P-Ti}_3\text{C}_2\text{T}_x$. (a) SEM of $\text{Ti}_3\text{C}_2\text{T}_x$; (b) SEM and (c) TEM images of $\text{P-Ti}_3\text{C}_2\text{T}_x$ (inset shows the HRTEM image along the [0001] zone axis); (d) FTIR spectra of $\text{Ti}_3\text{C}_2\text{T}_x$ and $\text{P-Ti}_3\text{C}_2\text{T}_x$; (e,f) EDS spectrum and element mapping images of $\text{P-Ti}_3\text{C}_2\text{T}_x$.

To further investigate the lattice structure of MXene, X-ray diffraction (XRD) and HRTEM characterization was conducted. As shown in Figure 2a, the characteristic (002) peak of $\text{Ti}_3\text{C}_2\text{T}_x$ shifted to a lower angle after the introduction of the P atom. According to the Bragg equation, the lattice spacing changes from 1.25 nm to 1.30 nm and 1.55 nm. The corresponding HRTEM images of $\text{P-Ti}_3\text{C}_2\text{T}_x$ (Figure 2b) also exhibit characteristic lattice fringe spaces of 1.55 nm of (002') and 1.30 nm of (002), which match well with the XRD results. The expansion of interlayer space should attribute to the successful insertion of

Na^+ and H_2PO_2^- in the layers of Ti_3C_2 during the ultrasonic treatment, which also leads to the $\text{P-Ti}_3\text{C}_2\text{T}_x$ exhibiting a larger BET specific surface area than pristine $\text{Ti}_3\text{C}_2\text{T}_x$ (Table S1). To exclude that the expansion of interlayer spacing is due to the annealing treatment, the XRD pattern of $\text{Ar-Ti}_3\text{C}_2\text{T}_x$ under the same conditions without $\text{NaH}_2\text{PO}_2 \cdot \text{H}_2\text{O}$ was also conducted. As shown in Figure S3, the (002) peak of $\text{Ar-Ti}_3\text{C}_2\text{T}_x$ moved to the right, indicating the expansion of interlayer spacing is not caused by heat treatment. The larger interlayer spacing and specific surface area favor undoubtedly the rapid diffusion of electrolyte ions and provide enough space to accommodate more electrolyte ions. Moreover, we noted that the characteristic peaks of TiO_2 (PDF# 21-1272) appear in $\text{Ar-Ti}_3\text{C}_2\text{T}_x$, and the TiO_2 with lower conductivity loses partial pseudocapacitance of the $\text{Ti}_3\text{C}_2\text{T}_x$ (Figure S3). Fortunately, due to the reductive nature of NaH_2PO_2 , MXene is not oxidized in the P doping process. In addition, the (002) peak of $\text{P-Ti}_3\text{C}_2\text{T}_x$ also splits into two peaks (002 and 002') as shown in Figure 2a. Here, we presume that the split-up of the (002) peak in $\text{P-Ti}_3\text{C}_2\text{T}_x$ is due to the partial decomposition of the intercalated H_2PO_2^- during annealing. Na^+ and H_2PO_2^- ions enter MXene interlayers in the ultrasonic process, expanding the interlayer spacing. Then, the partial decomposition of H_2PO_2^- during annealing makes the enlarged interlayer spacing become smaller. Even so, fortunately, $\text{P-Ti}_3\text{C}_2\text{T}_x$ still keeps larger interlayer spacing compared with that of pristine $\text{Ti}_3\text{C}_2\text{T}_x$. Figure 2c illustrates the structure evolution of $\text{Ti}_3\text{C}_2\text{T}_x$ during the preparation of $\text{P-Ti}_3\text{C}_2\text{T}_x$ and the phenomenon of (002) peak splitting.

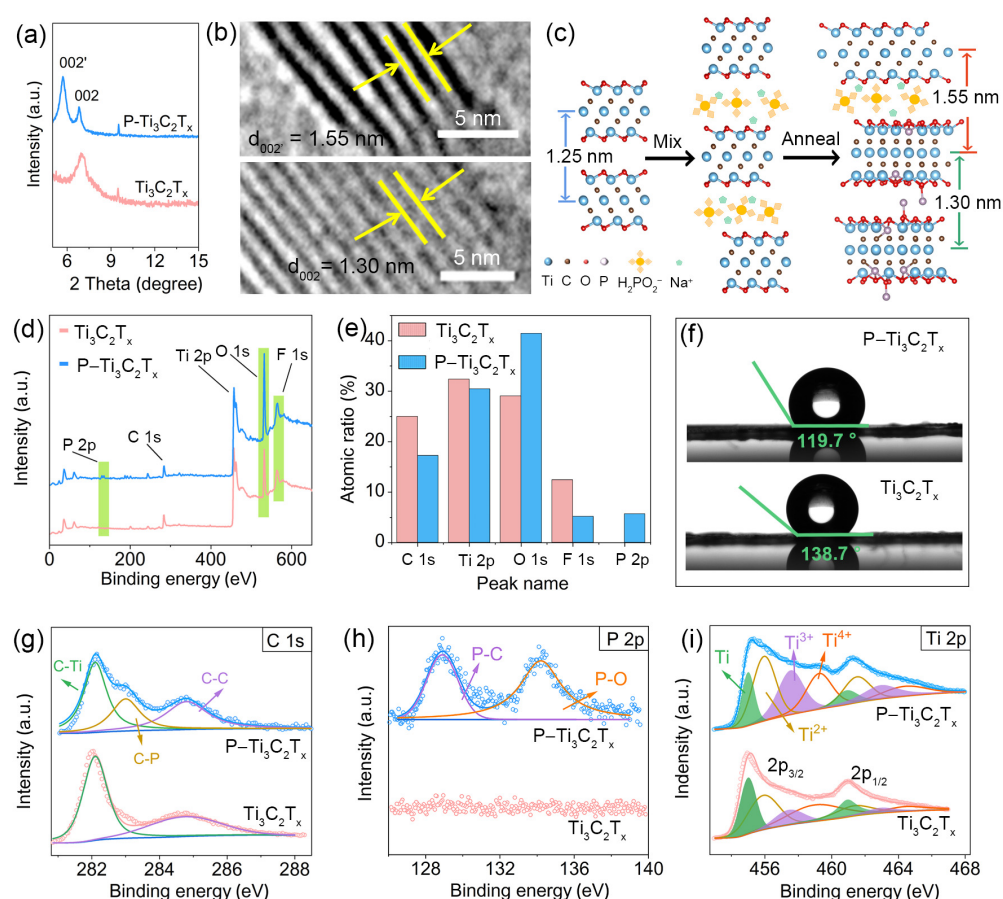


Figure 2. Characterization of the structure and chemical composition of $\text{Ti}_3\text{C}_2\text{T}_x$ and $\text{P-Ti}_3\text{C}_2\text{T}_x$. (a) XRD pattern of $\text{Ti}_3\text{C}_2\text{T}_x$ and $\text{P-Ti}_3\text{C}_2\text{T}_x$; (b) HRTEM images along the [1120] zone axis of $\text{P-Ti}_3\text{C}_2\text{T}_x$; (c) Structure model diagrams and corresponding schematic of the interlayer regulation in $\text{Ti}_3\text{C}_2\text{T}_x$; (d,e) Full XPS spectrum and corresponding different element proportions of $\text{Ti}_3\text{C}_2\text{T}_x$ and $\text{P-Ti}_3\text{C}_2\text{T}_x$; (f) Contact angle of water on $\text{Ti}_3\text{C}_2\text{T}_x$ and $\text{P-Ti}_3\text{C}_2\text{T}_x$; The corresponding high-resolution XPS spectra of (g) C 1s, (h) P 2p, (i) Ti 2p.

X-ray photoelectron spectroscopy (XPS) studies were then initiated to further investigate the change in component and valence states of $\text{Ti}_3\text{C}_2\text{T}_x$ MXene on P doping. The full XPS spectra of $\text{P-Ti}_3\text{C}_2\text{T}_x$ and $\text{Ti}_3\text{C}_2\text{T}_x$ shown in Figure 2d reveal that they all possess Ti, C, O, and F elements. Notably, the P peak appears in $\text{P-Ti}_3\text{C}_2\text{T}_x$, which proves the successful introduction of P atoms. The P atom is less electronegative and easily shares electrons with electrolyte ions (H^+), which is beneficial to charge storage. Moreover, the intensity of the F 1s peak decreased whereas the intensity of the O 1s peak increased after doping, suggesting that part of the fluorine group was detached from the surface of $\text{Ti}_3\text{C}_2\text{T}_x$ and replaced with oxygen-containing functional groups during the annealing treatment. This is consistent with the previous study that $-\text{F}$ is unstable and $-\text{O}$ is more stable [35]. The detailed change in atomic ratio of various elements in MXene is displayed in Figure 2e where after implementing the P doping strategy, the O atom content increased from 29.05% to 41.47%, and the F atom content decreased from 12.56% to 5.47%. To further confirm the variation in the surface functional groups of MXene, the surface contact angles of water on $\text{P-Ti}_3\text{C}_2\text{T}_x$ and pristine $\text{Ti}_3\text{C}_2\text{T}_x$ were tested, respectively. As shown in Figure 2f, the contact angle of water on $\text{P-Ti}_3\text{C}_2\text{T}_x$ considerably decreased due to the enhancement of the content of O-containing groups, which increases the hydrophilicity of MXene and is conducive to the contact between active sites and electrolyte ions, thus enhancing the electrochemical performance of the electrode. Based on the previously reported electrochemical reaction occurring in $\text{Ti}_3\text{C}_2\text{T}_x$ MXene [26]: $\text{Ti}_3\text{C}_2\text{O}_x(\text{OH})_y\text{F}_z + \delta\text{H}^+ + \delta\text{e}^- \leftrightarrow \text{Ti}_3\text{C}_2\text{O}_{x-\delta}(\text{OH})_{y+\delta}\text{F}_z$, we suppose that the reduction in the number of $-\text{F}$ functional groups and the increase in O-containing groups would greatly improve the capacitance [4].

High-resolution XPS can better analyze the change in the valence state of various atoms. From high-resolution XPS spectra of C 1s (Figure 2g), we can see that the $\text{Ti}_3\text{C}_2\text{T}_x$ shows two peaks around 282.1 eV and 284.8 eV corresponding to C-Ti and C-C [36], respectively. Interestingly, $\text{P-Ti}_3\text{C}_2\text{T}_x$ displays an additional C-P bond at 283.0 eV, which possibly is caused by P doping to the exposed edge of $\text{Ti}_3\text{C}_2\text{T}_x$ [37]. The P 2p spectrum is further studied to analyze the mechanism of P doping (Figure 2h). It can be observed that there is no P peak in the pristine $\text{Ti}_3\text{C}_2\text{T}_x$, while in the $\text{P-Ti}_3\text{C}_2\text{T}_x$ sample, two peaks appear. By Gaussian fitting, the P-C bond and P-O bond can be corresponding at 128.9 eV and 134.2 eV, respectively [26,37]. It means the P dopant can be attached to the surface of $\text{Ti}_3\text{C}_2\text{T}_x$ by adsorption/substitution. The presence of P-O groups would optimize the redox reaction process due to the lower electronegativity of the P atom. Moreover, the Ti 2p spectra obtained by Gaussian fitting are shown in Figure 2i. The Ti 2p_{3/2} spectra can be deconvoluted into four configurations, in which the binding energies are assigned to Ti (~455 eV), Ti^{2+} (~456 eV), Ti^{3+} (~457.6 eV), and Ti^{4+} (~459.3 eV) [36]. Furthermore, we can see that the content of the +3 valence state in $\text{P-Ti}_3\text{C}_2\text{T}_x$ (28.4%) is higher compared with $\text{Ti}_3\text{C}_2\text{T}_x$ (13.4%). The increase in valence may be due to the transition of the terminal group $-\text{F}$ to O-containing groups on the surface of $\text{Ti}_3\text{C}_2\text{T}_x$ and the introduction of P during annealing treatment. The higher valence can hold more electrons during the discharge process, thus increasing its specific capacitance [8].

2.2. Density Functional Theory Calculations

To better understand the effect of P doping on the properties of MXene, we conducted theoretical calculations of the electronic structure before and after P doping. A supercell of $\text{Ti}_3\text{C}_2\text{O}_2$ was constructed as the initial calculated model because O is the dominant functional group after annealing treatment (Figure 3a). Furthermore, according to the atomic ratio of P/Ti in the XPS result and the proportion of P-O and P-C bonds in P 2p spectra (Figure 2e,h), five Ti atoms are substituted by five P atoms, and the other three P atoms are bonded with O atoms directly in the supercell to approximate the P atoms concentration in $\text{P-Ti}_3\text{C}_2\text{T}_x$. The constructed structure denoted as $\text{P-Ti}_3\text{C}_2\text{O}_2$ is shown in Figure 3a. Figure 3b displays the total density of states (TDOS) of $\text{P-Ti}_3\text{C}_2\text{O}_2$ and $\text{Ti}_3\text{C}_2\text{O}_2$, respectively. The modulation of electronic configuration and spin polarization leads to the variation of DOS curves of $\text{P-Ti}_3\text{C}_2\text{O}_2$ for both the up-spin and down-spin states. Both

$\text{Ti}_3\text{C}_2\text{O}_2$ and $\text{P-Ti}_3\text{C}_2\text{O}_2$ display non-zero peaks across the Fermi level, which implies they possess zero band gaps. Notably, the $\text{P-Ti}_3\text{C}_2\text{O}_2$ has higher DOS whether at the valence band (VB) or at the conduction band (CB) across the Fermi level, manifesting that electrons could easily migrate from VB to CB, implying the enhanced electronic conductivity of $\text{P-Ti}_3\text{C}_2\text{O}_2$. As the partial density of states (PDOS) of $\text{P-Ti}_3\text{C}_2\text{O}_2$ and $\text{Ti}_3\text{C}_2\text{O}_2$ shown (Figures 3c and S4), CB of $\text{Ti}_3\text{C}_2\text{O}_2$ and $\text{P-Ti}_3\text{C}_2\text{O}_2$ is mainly contributed by Ti 3d, while the VB originates from the hybridization of Ti 3d, C 2p and O 2p. Moreover, the P atom made a considerable contribution to DOS at the Fermi level, leading to $\text{P-Ti}_3\text{C}_2\text{O}_2$ owning much higher electronic conductivity.

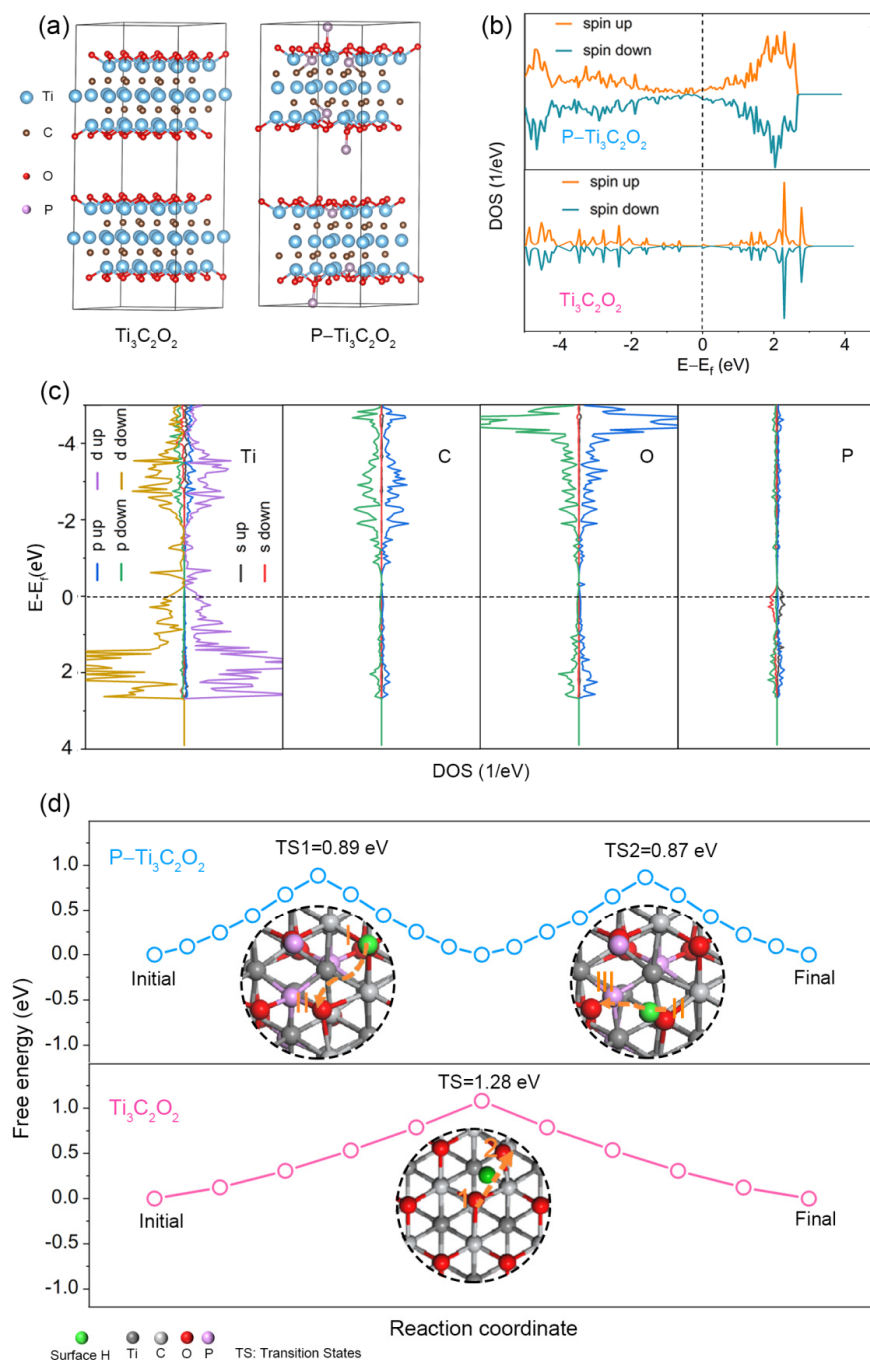


Figure 3. Calculation results based on DFT for $\text{P-Ti}_3\text{C}_2\text{O}_2$ and $\text{Ti}_3\text{C}_2\text{O}_2$. (a) Model structure of $\text{Ti}_3\text{C}_2\text{O}_2$ and $\text{P-Ti}_3\text{C}_2\text{O}_2$; (b) TDOS of $\text{P-Ti}_3\text{C}_2\text{O}_2$ and $\text{Ti}_3\text{C}_2\text{O}_2$; (c) PDOS of $\text{P-Ti}_3\text{C}_2\text{O}_2$; (d) Diffusion free energy of H diffusion along different paths on the $\text{P-Ti}_3\text{C}_2\text{O}_2$ and $\text{Ti}_3\text{C}_2\text{O}_2$ surfaces.

The migration and diffusion of electrolyte ion H^+ in electrode materials also affect the electrochemical performance of electrode materials. The calculation results based on the DFT of the free energy for hydrogen atoms diffusion on $Ti_3C_2O_2$ and $P-Ti_3C_2O_2$ surfaces in different paths are shown in Figure 3d. (Optimization model structures of H diffusion on the surface of $P-Ti_3C_2O_2$ and $Ti_3C_2O_2$ and the detailed diffusion process are shown in Figure S5). Surface H prefers to attach to oxygen atoms on the surface of MXene, so the possible path for H diffusion is chosen between the two nearest O sites. For $Ti_3C_2O_2$, the surface H directly diffuses from one O site to the nearest O site, that is, from site 1 to 2, and the diffusion free energy is 1.28 eV. For $P-Ti_3C_2O_2$, we choose two possible paths for the diffusion of H on the surface taking into the effect of P doping, i.e., H diffuses from site I to II, or from site II to III. The diffusion free energies for both paths are 0.89 and 0.87 eV, respectively, which is lower than that in $Ti_3C_2O_2$. The lower diffusion free energy undoubtedly facilitates the diffusion of electrolyte ions on the electrode material surface.

2.3. Electrochemical Performances of Electrodes

To verify the practical effect of the change in the interlayer spacing and the introduction of doped P atoms on the electrochemical performance, we first performed CV tests of $Ti_3C_2T_x$ and $P-Ti_3C_2T_x$ in 1 M H_2SO_4 solution. In Figure 4a, the CV curves of all samples display a rectangular shape, showing capacitive behavior, in which $P-Ti_3C_2T_x$ has a greater current response. Noticeably, a pair of weak peaks in low voltage (around -0.15 V) appear in the CV curves of the $P-Ti_3C_2T_x$ electrode, which may be due to the Faraday reaction caused by the doped P atom because it is less electronegative and prefers to share electrons with H; consequently, it can take part in reaction at relatively low voltages. The specific capacitance at different scan rates calculated by CV curves is shown in Figure 4b. The specific capacitance of $P-Ti_3C_2T_x$ reached 510 F g^{-1} at 2 mV s^{-1} , which is higher than that of most reported similar electrode materials, including $P-Ti_3C_2T_x$, N-doped $Ti_3C_2T_x$ and N, P-doped graphene (Table S2). At the scan rate of 100 mV s^{-1} , the CV curve of $P-Ti_3C_2T_x$ has no obvious distortion (Figure 4c), and it still delivers a capacitance of 400 F g^{-1} (Figure 4b), capacitance retention maintaining 78% from 2 mV s^{-1} to 100 mV s^{-1} , which is higher than 35% of pristine $Ti_3C_2T_x$. To eliminate the influence of annealing, $Ar-Ti_3C_2T_x$ was synthesized under the same condition without NaH_2PO_2 . As shown in Figure S6, $Ar-Ti_3C_2T_x$ delivers a minimum electrochemical response area at the same scan rate, that is, it has the smallest specific capacitance, which may be due to the formation of TiO_2 in the annealing treatment process without NaH_2PO_2 with reductive nature.

EIS data can help us investigate the electrical conductivity, charge transfer kinetics, and ion diffusion properties of the electrode. In EIS plots, the high-frequency semicircle diameter is related to the charge transfer resistance (R_{ct}) and the diagonal line in the low-frequency region shows charge storage behavior. As shown in Figure 4d and Table S3, $P-Ti_3C_2T_x$ possesses lower R_{ct} than pure $Ti_3C_2T_x$ and a higher value of fractional exponent α of constant phase element (CPE), suggesting that $P-Ti_3C_2T_x$ has a higher electrical conductivity and a more rapid ion diffusion path. This is consistent with the above results for the DOS and H diffusion free energies analysis. Figure 4e shows that $P-Ti_3C_2T_x$ possesses a smaller characteristic relaxation time constant of τ_0 ($\tau_0 = f_0^{-1}$), proving the high-rate performance of $P-Ti_3C_2T_x$ [38–40].

For supercapacitors, the long cycle stability of the electrode is one of the key points, because the specific capacitance of the device over time depends on it. Figure 4f exhibits the extended GCD tests approaching 10,000 cycles at a high current density of 20 A g^{-1} for $P-Ti_3C_2T_x$. Notably, after 10,000 cycles, $P-Ti_3C_2T_x$ still remains at 90.2% of initial capacitance, which is higher than that of pristine $Ti_3C_2T_x$ (81.3%, Figure S7) and its Coulombic efficiency of $P-Ti_3C_2T_x$ is close to 100% in the whole cycles. The enhanced cycle stability may be due to the expanded interlayer space, which allows rapid insertion and removal of electrolyte ions without obvious structure change during the charge–discharge processes.

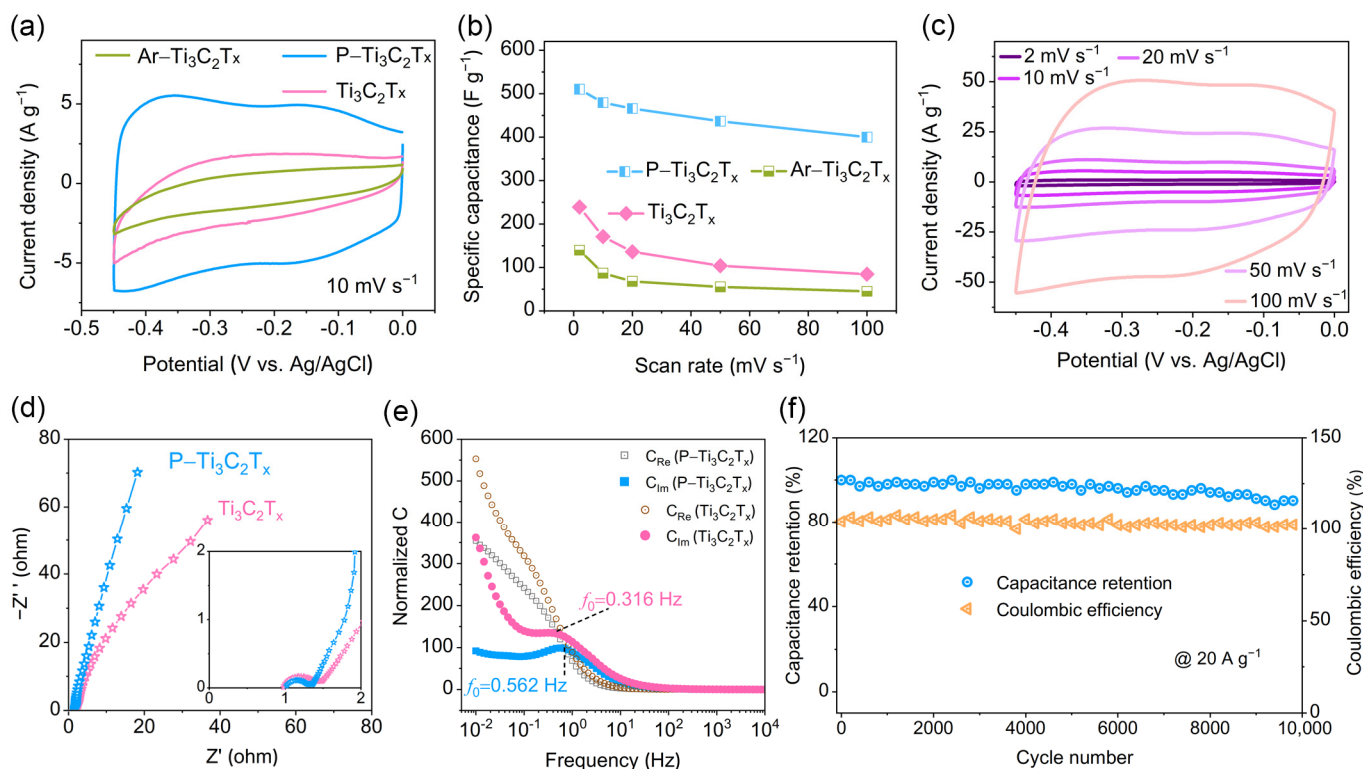


Figure 4. Electrochemical performance. (a) CV profiles of $\text{Ti}_3\text{C}_2\text{T}_x$, $\text{P-Ti}_3\text{C}_2\text{T}_x$, and $\text{Ar-Ti}_3\text{C}_2\text{T}_x$; (b) Specific capacitance of $\text{Ti}_3\text{C}_2\text{T}_x$, $\text{P-Ti}_3\text{C}_2\text{T}_x$, and $\text{Ar-Ti}_3\text{C}_2\text{T}_x$ calculated by their CV curves; (c) CV curves of $\text{P-Ti}_3\text{C}_2\text{T}_x$ at different scan rate; (d) EIS plots of $\text{Ti}_3\text{C}_2\text{T}_x$ and $\text{P-Ti}_3\text{C}_2\text{T}_x$; (e) Normalized real (C_{Re}) and imaginary (C_{Im}) parts of capacitance versus frequency of $\text{Ti}_3\text{C}_2\text{T}_x$ and $\text{P-Ti}_3\text{C}_2\text{T}_x$; (f) Cyclic stability of $\text{P-Ti}_3\text{C}_2\text{T}_x$ for 10,000 cycles at the current density of 20 A g^{-1} .

To gain insight into the charge storage mechanism of the electrodes, the surface capacitive contribution and the diffusion control contribution are analyzed. First, we plotted the $\log i$ - $\log v$ curve, using Formula [41]:

$$\log i = b \cdot \log v + \log a$$

where i and v present currents under various voltage and scan rates of CV curves, respectively. b and a present slope of the $\log i$ - $\log v$ plot and constant. Figure 5a displays the b -values of $\text{P-Ti}_3\text{C}_2\text{T}_x$ and $\text{Ti}_3\text{C}_2\text{T}_x$ as calculated at different voltages corresponding to the CV curves. It is clear that $\text{P-Ti}_3\text{C}_2\text{T}_x$ owns higher b values (closed to 1) than pure $\text{Ti}_3\text{C}_2\text{T}_x$ (closed to 0.5), indicating $\text{P-Ti}_3\text{C}_2\text{T}_x$ shows a surface-controlled charge storage behavior in the electrochemical processes whereas the electrochemical processes of pristine $\text{Ti}_3\text{C}_2\text{T}_x$ are dominated by diffusion-controlled charge storage behavior. More specifically, the contribution proportion of the two mechanisms in total capacitance can be quantitatively distinguished at a randomizing scan rate according to the following Formula [42]:

$$i(V) = k_1 \cdot v + k_2 \cdot v^{1/2}$$

where $i(V)$ corresponds to the current at the specific voltage, v stands for the scan rate, $k_1 \cdot v$ and $k_2 \cdot v^{1/2}$ represent the surface capacitive control and the diffusion control, respectively. The results show that the proportion of surface capacitive contribution increases with the increase in scan rates for both electrodes (Figures 5b,c, S8 and S9). Notably, the proportion of the surface capacitive contribution of $\text{P-Ti}_3\text{C}_2\text{T}_x$ is always larger than that of pure $\text{Ti}_3\text{C}_2\text{T}_x$ at various scan rates, which is consistent with the b -value analysis results. The high surface capacitance contribution implies that there is a fast ion diffusion in $\text{P-Ti}_3\text{C}_2\text{T}_x$, which is

mainly due to the expanded interlayer spacing and lower diffusion free energy in $P\text{-Ti}_3\text{C}_2\text{T}_x$. We can also understand the electrochemical process of $P\text{-Ti}_3\text{C}_2\text{T}_x$ MXene from the in situ electrochemical EIS results. Figure S10 shows the in situ EIS diagram during the discharge process. In the low-frequency range of Nyquist plots around open circuit potential (-0.02 V), the curve is characterized by a diagonal. When the voltage changes from -0.02 V to -0.06 V, the imaginary part of the impedance rises sharply (almost vertically), indicating that the inserted hydrated cation increases the interlayer spacing, resulting in fast and free ion transport. As the discharge reaction proceeds, the diagonals of the EIS plots are always approximately perpendicular, indicating a uniform and expanded interlayer space exists in $P\text{-Ti}_3\text{C}_2\text{T}_x$, which improves ion accessibility to the active site, resulting in high specific energy storage capacity. Here, the decrease in impedance imaginary part value from -0.06 V to -0.25 V should be attributed to the continuous accumulation of charge.

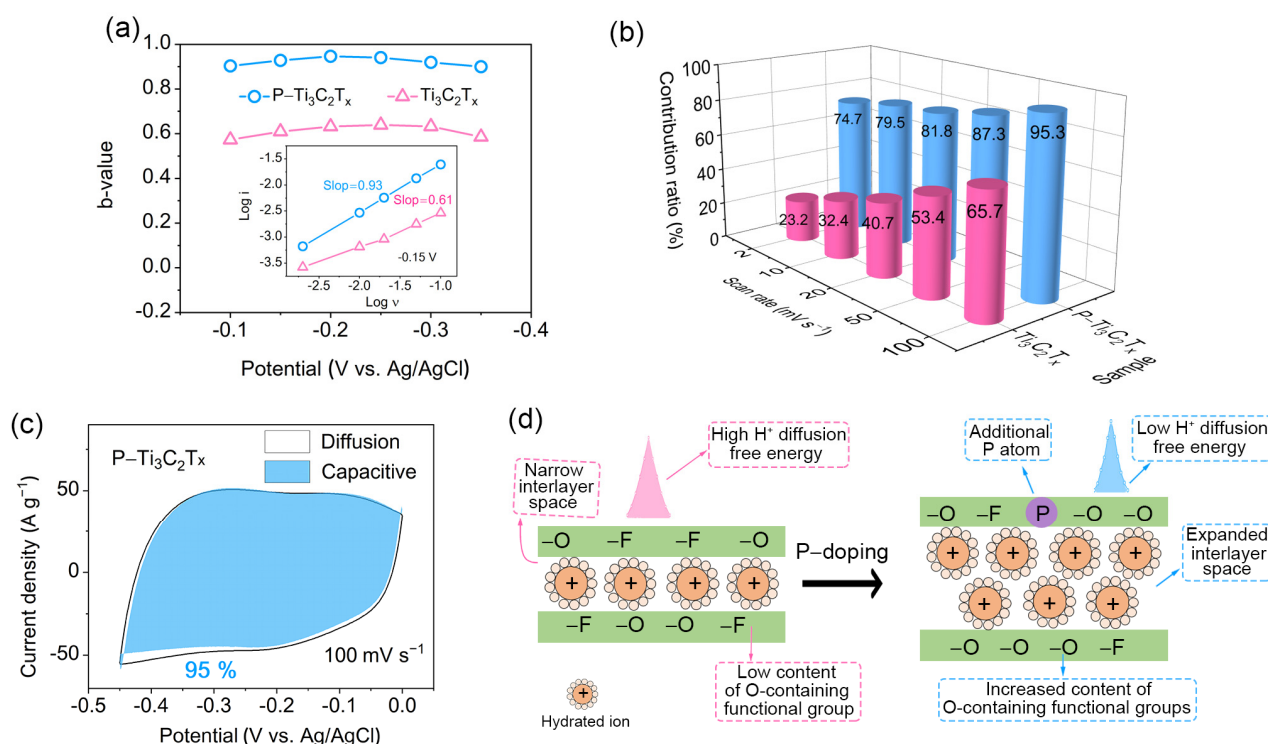


Figure 5. The charge storage mechanism of $P\text{-Ti}_3\text{C}_2\text{T}_x$ and $\text{Ti}_3\text{C}_2\text{T}_x$. (a) The b values of $P\text{-Ti}_3\text{C}_2\text{T}_x$ and $\text{Ti}_3\text{C}_2\text{T}_x$; (b) Comparison plot between $\text{Ti}_3\text{C}_2\text{T}_x$ (pink) and $P\text{-Ti}_3\text{C}_2\text{T}_x$ (blue) of the normalized contribution of capacitive at various scan rates; (c) CV data of $P\text{-Ti}_3\text{C}_2\text{T}_x$ corresponding to the capacitive contribution for the total current at 100 mV s^{-1} ; (d) Schematic illustration of charge storage of hydrated electrolyte ions in $\text{Ti}_3\text{C}_2\text{T}_x$ and $P\text{-Ti}_3\text{C}_2\text{T}_x$.

As discussed above, the enhanced electrochemical performance should be ascribed to several reasons as follows (Figure 5d). The expansion of interlayer spacing facilitates rapid H^+ transport. The increased content of O-containing functional groups increases the hydrophilicity of the electrode, which is conducive to the contact of MXene surface with the electrolyte and thus increases active site accessibility. The increase in O-containing functional groups provides more active sites and the doped P atoms bring additional active sites, which greatly increase the specific capacitance. The change in surface functional groups causes the increase in Ti content of the high valence state with an electrochemical activity that can accommodate more electrons during discharge. Moreover, the introduction of P increases the electrical conductivity of MXene and reduces the free energy of H^+ diffusion on the MXene surface, which is conducive to electrochemical reactions.

3. Experiment

3.1. Synthesis of Pristine $Ti_3C_2T_x$ MXene

The $Ti_3C_2T_x$ MXene was prepared by etching Al layer from Ti_3AlC_2 MAX phase which was prepared in the house laboratory by the solid–liquid reaction synthesis method [43] (Figures S1 and S2). In detail, 3 g Ti_3AlC_2 powder was slowly added into 60 mL etching solution (9 M HCl, 12 M LiF) at room temperature for 20 days to remove the Al layer. The suspension was drained by vacuum filtration and the sediment was washed with 1 M HCl followed by deionized water until the pH reached 6. Finally, the obtained product was dried at 60 °C overnight to produce $Ti_3C_2T_x$ powder.

3.2. Synthesis of P- $Ti_3C_2T_x$ and Ar- $Ti_3C_2T_x$

The P- $Ti_3C_2T_x$ was fabricated by annealing a mixture of $Ti_3C_2T_x$ powder and $NaH_2PO_2 \cdot H_2O$. In brief, 200 mg $Ti_3C_2T_x$ powder was mixed with 20 mL DI water to form a suspension under ultra-sonic treatment for 5 min, and then 2 g $NaH_2PO_2 \cdot H_2O$ was dissolved in the above suspension. Then, the mixed solution was freeze-dried, placed in a tube furnace, and annealed under Ar flow at 400 °C for 2 h with a heating rate of 2 °C min^{-1} . Finally, the resulting product was rinsed with DI water to remove the resultant phosphate salts. Ar- $Ti_3C_2T_x$ was prepared under the same condition without $NaH_2PO_2 \cdot H_2O$.

3.3. Material Characterizations

The microstructure morphology and element distribution were characterized using a JEOL JSM-6700F (JEOL Japan Electronics Co., Ltd., Tokyo, Japan) field emission FESEM equipped with EDS equipment. More detailed structural information was acquired by using a JEM-2100PLUS (JEOL Japan Electronics Co., Ltd.) TEM equipment. The FTIR spectroscopy was performed on a Nicolet IS10 (Thermo Fisher Scientific, Waltham, MA, USA) device. The XRD pattern of the samples was recorded using a Rigaku MiniFlex (Rigaku Corporation, Tokyo, Japan) X-ray diffractometer. N_2 adsorption–desorption tests were performed using Micromeritics ASAP2460-2 (Micromeritics Instruments Corporation, Norcross, GA, USA). The XPS spectra analysis was performed to further characterize the chemical compositions on a Thermo ESCALAB Xi⁺ (Thermo Fisher Scientific (China) Co., Ltd., Shanghai, China) device with an Al-K α excitation source.

3.4. Computational Detail

Density functional theory (DFT) was performed by Vienna Ab-initio Simulation Package (VASP) software [44] with the projector augmented wave (PAW) method [45]. The convergence threshold of energy was set as 10^{-5} eV and the convergence threshold of maximum stress was 0.05 eV/Å. The cut-off energy was set as 400 eV, and the k-points were $2 \times 2 \times 1$. Hubbard U correction was set, and the U value was 4.0 eV for 3d orbit Ti.

3.5. Electrochemical Measurements

Electrochemical performance tests were carried out in a three-electrode system on an electrochemical workstation (CHI 660E, Shanghai Chenhua Instrument Co., Shanghai, China) at room temperature, where Ag/AgCl, Pt wire, and 1 M H_2SO_4 solution as reference electrode, counter electrode, and electrolyte, respectively. For working electrode, a mixture of 80 wt% active material, 10 wt% polyvinylidene fluoride, and 10 wt% carbon black in N-methyl pyrrolidone was ground in an agate mortar until the slurry was grain-free, and then coated on copper foil and dried at 60 °C for 12 h. The electrochemical performances were studied by cyclic voltammetry (CV) and electrochemical impedance spectroscopy (EIS) techniques.

4. Conclusions

In summary, P-doped $Ti_3C_2T_x$ MXene was prepared by a simple annealing method with NaH_2PO_2 as phosphorus source, which delivers a high specific capacitance of 510 $F g^{-1}$ and 400 $F g^{-1}$ at the scan rate of 2 $mV s^{-1}$ and 100 $mV s^{-1}$. Morphology and component

characterization, DFT calculation, and electrochemical kinetic analysis have been used to give deep insight into the mechanism of improvement in electrochemical performance. The expansion of interlayer spacing facilitates rapid H^+ transport. The increased content of O-containing functional groups and the introduction of P atoms not only increase the hydrophilicity of the electrode material but also bring more active sites. The change in surface functional groups causes the increase in Ti content of the high valence state with a higher electrochemical activity that can accommodate more electrons during discharge. Moreover, the introduction of P improves the electrical conductivity of MXene and reduces the free energy of H^+ diffusion on the MXene surface. Synergistic modification of interlayer structure and chemical state improves the possibility of $Ti_3C_2T_x$ for accommodating more H^+ ions. This work opens avenues for the development of other 2D materials in constructing high-energy storage systems by heterogeneous atom doping.

Supplementary Materials: The following supporting information can be downloaded at: <https://www.mdpi.com/article/10.3390/molecules28134892/s1>, Figure S1: The $Ti_3C_2T_x$ MXene was prepared from Ti_3AlC_2 MAX phase by etching Al layer; Figure S2: (a) SEM image and (b) XRD pattern of Ti_3AlC_2 MAX phase particles; Figure S3: XRD pattern of $Ti_3C_2T_x$, Ar- $Ti_3C_2T_x$ and P- $Ti_3C_2T_x$; Figure S4: PDOS of $Ti_3C_2T_x$; Figure S5: Optimization model structures of H diffusion on the surface of (a) P- $Ti_3C_2O_2$ and (b) $Ti_3C_2O_2$ and the detailed diffusion process; Figure S6: CV profiles of (a) $Ti_3C_2T_x$ and (b) Ar- $Ti_3C_2T_x$. The area of CV curves of both samples increases with the increase in scan rate; Figure S7: Cyclic stability of $Ti_3C_2T_x$ for 10,000 cycles at the current density of $20 A g^{-1}$; Figure S8: Kinetic and quantitative analysis of the P- $Ti_3C_2T_x$ electrode; Figure S9: Kinetic and quantitative analysis of the $Ti_3C_2T_x$ electrode; Figure S10: In situ EIS spectra of P- $Ti_3C_2T_x$ electrodes; Table S1: BET specific surface area of the electrode materials; Table S2: Comparison of electrochemical performance between P- $Ti_3C_2T_x$ and previously reported heteroatom-doped MXene electrodes [26–28,31,37,46]; Table S3: EIS fitting results of $Ti_3C_2T_x$ and P- $Ti_3C_2T_x$.

Author Contributions: Conceptualization, Z.L., C.S., A.M. and M.H.; formal analysis, C.S. and A.M.; funding acquisition, Z.L. and M.H.; investigation, Y.B., Y.J. and J.D.; methodology, L.C., Y.B., Y.J. and J.D.; project administration, Z.L.; software, H.X.; supervision, Z.L. and M.H.; writing—original draft, L.C.; writing—review and editing, M.H. All authors have read and agreed to the published version of the manuscript.

Funding: The work reported here was supported by the National Natural Science Foundation of China under Grant Nos. 52072196, 52002200, 52102106, Major Basic Research Program of Natural Science Foundation of Shandong Province under Grant No. ZR2020ZD09, the Natural Science Foundation of Shandong Province under Grant Nos. ZR2019BEM042, ZR2020QE063, the Innovation and Technology Program of Shandong Province under Grant No. 2020KJA004, the Open Project of Chemistry Department of Qingdao University of Science and Technology under Grant No. QUSTHX201813, and the Taishan Scholars Program of Shandong Province under No. ts201511034. We express our grateful thanks to them for their financial support.

Institutional Review Board Statement: Not applicable.

Informed Consent Statement: Not applicable.

Data Availability Statement: Not applicable.

Acknowledgments: We also thank the researchers who facilitated the completion of this study.

Conflicts of Interest: The authors declare no conflict of interest.

Sample Availability: Not applicable.

Safety Statement: As for the synthesis of P- $Ti_3C_2T_x$, the toxic gas PH_3 is released during the heat treatment process. Therefore, an exhaust gas treatment device must be equipped.

References

1. Zhu, Q.; Zhao, D.; Cheng, M.; Zhou, J.; Owusu, K.A.; Mai, L.; Yu, Y. A new view of supercapacitors: Integrated supercapacitors. *Adv. Energy Mater.* **2019**, *9*, 1901081. [[CrossRef](#)]
2. Sun, C.; Wang, Y.-J.; Gu, H.; Fan, H.; Yang, G.; Ignaszak, A.; Tang, X.; Liu, D.; Zhang, J. Interfacial coupled design of epitaxial Graphene@SiC Schottky junction with built-in electric field for high-performance anodes of lithium ion batteries. *Nano Energy* **2020**, *77*, 105092. [[CrossRef](#)]
3. Wang, T.; Chen, H.C.; Yu, F.; Zhao, X.S.; Wang, H. Boosting the cycling stability of transition metal compounds-based supercapacitors. *Energy Stor. Mater.* **2019**, *16*, 545–573. [[CrossRef](#)]
4. Li, Z.; Dai, J.; Li, Y.; Sun, C.; Meng, A.; Cheng, R.; Zhao, J.; Hu, M.; Wang, X. Intercalation-deintercalation design in MXenes for high-performance supercapacitors. *Nano Res.* **2022**, *15*, 3213–3221. [[CrossRef](#)]
5. Rehman, J.; Eid, K.; Ali, R.; Fan, X.; Murtaza, G.; Faizan, M.; Laref, A.; Zheng, W.; Varma, R.S. Engineering of transition metal sulfide nanostructures as efficient electrodes for high-performance supercapacitors. *ACS Appl. Energy Mater.* **2022**, *5*, 6481–6498. [[CrossRef](#)]
6. Zhang, L.L.; Zhao, X.S. Carbon-based materials as supercapacitor electrodes. *Chem. Soc. Rev.* **2009**, *38*, 2520–2531. [[CrossRef](#)]
7. Dou, Q.; Wu, N.; Yuan, H.; Shin, K.H.; Tang, Y.; Mitlin, D.; Park, H.S. Emerging trends in anion storage materials for the capacitive and hybrid energy storage and beyond. *Chem. Soc. Rev.* **2021**, *50*, 6734–6789. [[CrossRef](#)]
8. Hu, M.; Dai, J.; Chen, L.; Meng, A.; Wang, L.; Li, G.; Xie, H.; Li, Z. Selectivity for intercalated ions in MXene toward a high-performance capacitive electrode. *Sci. China Mater.* **2023**, *66*, 974–981. [[CrossRef](#)]
9. Xu, J.; Yang, N.; Heuser, S.; Yu, S.; Schulte, A.; Schönherr, H.; Jiang, X. Achieving ultrahigh energy densities of supercapacitors with porous titanium carbide/boron-doped diamond composite electrodes. *Adv. Energy Mater.* **2019**, *9*, 1803623. [[CrossRef](#)]
10. Lin, Z.; Goikolea, E.; Balducci, A.; Naoi, K.; Taberna, P.L.; Salanne, M.; Yushin, G.; Simon, P. Materials for supercapacitors: When Li-ion battery power is not enough. *Mater. Today* **2018**, *21*, 419–436. [[CrossRef](#)]
11. Dillon, A.D.; Ghidui, M.J.; Krick, A.L.; Griggs, J.; May, S.J.; Gogotsi, Y.; Barsoum, M.W.; Fafarman, A.T. Highly conductive optical quality solution-processed films of 2D titanium carbide. *Adv. Funct. Mater.* **2016**, *26*, 4162–4168. [[CrossRef](#)]
12. Zhang, C.; Ma, Y.; Zhang, X.; Abdolhosseinzadeh, S.; Sheng, H.; Lan, W.; Pakdel, A.; Heier, J.; Nüesch, F. Two-dimensional transition metal carbides and nitrides (MXenes): Synthesis, properties, and electrochemical energy storage applications. *Energy Environ. Mater.* **2020**, *3*, 29–55. [[CrossRef](#)]
13. Hui, X.; Ge, X.; Zhao, R.; Li, Z.; Yin, L. Interface chemistry on MXene-based materials for enhanced energy storage and conversion performance. *Adv. Funct. Mater.* **2020**, *30*, 2005190. [[CrossRef](#)]
14. Li, K.; Liang, M.; Wang, H.; Wang, X.; Huang, Y.; Coelho, J.; Pinilla, S.; Zhang, Y.; Qi, F.; Nicolosi, V.; et al. 3D MXene architectures for efficient energy storage and conversion. *Adv. Funct. Mater.* **2020**, *30*, 2000842. [[CrossRef](#)]
15. Zhu, Y.; Zheng, S.; Lu, P.; Ma, J.; Das, P.; Su, F.; Cheng, H.-M.; Wu, Z.-S. Kinetic regulation of MXene with water-in-LiCl electrolyte for high-voltage micro-supercapacitors. *Natl. Sci. Rev.* **2022**, *9*, nwac024. [[CrossRef](#)]
16. Zhu, Y.; Zheng, S.; Qin, J.; Ma, J.; Das, P.; Zhou, F.; Wu, Z.-S. 2.4 V ultrahigh-voltage aqueous MXene-based asymmetric micro-supercapacitors with high volumetric energy density toward a self-sufficient integrated microsystem. *Fundam. Res.* **2022**. [[CrossRef](#)]
17. Ibrahim, Y.; Mohamed, A.; Abdelgawad, A.M.; Eid, K.; Abdullah Aboubakr, M.; Elzatahry, A. The recent advances in the mechanical properties of self-standing two-dimensional MXene-based nanostructures: Deep insights into the supercapacitor. *Nanomaterials* **2020**, *10*, 1916. [[CrossRef](#)]
18. Scheibe, B.; Tadzysak, K.; Jarek, M.; Michalak, N.; Kempniński, M.; Lewandowski, M.; Peplińska, B.; Chybczyńska, K. Study on the magnetic properties of differently functionalized multilayered Ti₃C₂T_x MXenes and Ti-Al-C carbides. *Appl. Surf. Sci.* **2019**, *479*, 216–224. [[CrossRef](#)]
19. Lin, Z.; Shao, H.; Xu, K.; Taberna, P.-L.; Simon, P. MXenes as high-rate electrodes for energy storage. *Trends Chem.* **2020**, *2*, 654–664. [[CrossRef](#)]
20. Eid, K.; Lu, Q.; Abdel-Azeim, S.; Soliman, A.; Abdullah, A.M.; Abdelgwad, A.M.; Forbes, R.P.; Ozoemena, K.I.; Varma, R.S.; Shibl, M.F. Highly exfoliated Ti₃C₂T_x MXene nanosheets atomically doped with Cu for efficient electrochemical CO₂ reduction: An experimental and theoretical study. *J. Mater. Chem. A* **2022**, *10*, 1965–1975. [[CrossRef](#)]
21. Ma, J.; Cheng, Y.; Wang, L.; Dai, X.; Yu, F. Free-standing Ti₃C₂T_x MXene film as binder-free electrode in capacitive deionization with an ultrahigh desalination capacity. *Chem. Eng. J.* **2020**, *384*, 123329. [[CrossRef](#)]
22. Bai, Y.; Liu, C.; Chen, T.; Li, W.; Zheng, S.; Pi, Y.; Luo, Y.; Pang, H. MXene-copper/cobalt hybrids via Lewis acidic molten salts etching for high performance symmetric supercapacitors. *Angew. Chem. Int. Ed.* **2021**, *60*, 25318–25322. [[CrossRef](#)] [[PubMed](#)]
23. Zhu, Y.; Wang, S.; Ma, J.; Das, P.; Zheng, S.; Wu, Z.-S. Recent status and future perspectives of 2D MXene for micro-supercapacitors and micro-batteries. *Energy Stor. Mater.* **2022**, *51*, 500–526. [[CrossRef](#)]
24. Zhu, Y.; Ma, J.; Das, P.; Wang, S.; Wu, Z.-S. High-voltage MXene-based supercapacitors: Present status and future perspectives. *Small Methods* **2023**, 2201609. [[CrossRef](#)] [[PubMed](#)]
25. Hu, M.; Zhang, H.; Hu, T.; Fan, B.; Wang, X.; Li, Z. Emerging 2D MXenes for supercapacitors: Status, challenges and prospects. *Chem. Soc. Rev.* **2020**, *49*, 6666–6693. [[CrossRef](#)]
26. Gupta, N.; Sahu, R.K.; Mishra, T.; Bhattacharya, P. Microwave-assisted rapid synthesis of titanium phosphate free phosphorus doped Ti₃C₂ MXene with boosted pseudocapacitance. *J. Mater. Chem. A* **2022**, *10*, 15794–15810. [[CrossRef](#)]

27. Wen, Y.; Rufford, T.E.; Chen, X.; Li, N.; Lyu, M.; Dai, L.; Wang, L. Nitrogen-doped $Ti_3C_2T_x$ MXene electrodes for high-performance supercapacitors. *Nano Energy* **2017**, *38*, 368–376. [[CrossRef](#)]
28. Zhang, T.; Xiao, J.; Li, L.; Zhao, J.; Gao, H. A high-performance supercapacitor electrode based on freestanding N-doped $Ti_3C_2T_x$ film. *Ceram. Int.* **2020**, *46*, 21482–21488. [[CrossRef](#)]
29. Pu, L.; Zhang, J.; Jiresse, N.K.L.; Gao, Y.; Zhou, H.; Naik, N.; Gao, P.; Guo, Z. N-doped MXene derived from chitosan for the highly effective electrochemical properties as supercapacitor. *Adv. Compos. Hybrid Mater.* **2022**, *5*, 356–369. [[CrossRef](#)]
30. Lin, G.; Wang, Q.; Yang, X.; Cai, Z.; Xiong, Y.; Huang, B. Preparation of phosphorus-doped porous carbon for high performance supercapacitors by one-step carbonization. *RSC Adv.* **2020**, *10*, 17768–17776. [[CrossRef](#)]
31. Wen, Y.; Rufford, T.E.; Hulicova-Jurcakova, D.; Wang, L. Nitrogen and phosphorous co-doped graphene monolith for supercapacitors. *ChemSusChem* **2016**, *9*, 513–520. [[CrossRef](#)]
32. Cai, M.; Yan, H.; Li, Y.; Li, W.; Li, H.; Fan, X.; Zhu, M. $Ti_3C_2T_x$ /PANI composites with tunable conductivity towards anticorrosion application. *Chem. Eng. J.* **2021**, *410*, 128310. [[CrossRef](#)]
33. Qin, Y.; Wang, Z.; Liu, N.; Sun, Y.; Han, D.; Liu, Y.; Niu, L.; Kang, Z. High-yield fabrication of $Ti_3C_2T_x$ MXene quantum dots and their electrochemiluminescence behavior. *Nanoscale* **2018**, *10*, 14000–14004. [[CrossRef](#)] [[PubMed](#)]
34. Hui, X.; Zhao, R.; Zhang, P.; Li, C.; Wang, C.; Yin, L. Low-temperature reduction strategy dyanthesized Si/ Ti_3C_2 MXene composite anodes for high-performance Li-ion batteries. *Adv. Energy Mater.* **2019**, *9*, 1901065. [[CrossRef](#)]
35. Hu, T.; Li, Z.; Hu, M.; Wang, J.; Hu, Q.; Li, Q.; Wang, X. Chemical origin of termination-functionalized MXenes: $Ti_3C_2T_2$ as a case study. *J. Phys. Chem. C* **2017**, *121*, 19254–19261. [[CrossRef](#)]
36. Halim, J.; Cook, K.M.; Naguib, M.; Eklund, P.; Gogotsi, Y.; Rosen, J.; Barsoum, M.W. X-ray photoelectron spectroscopy of select multi-layered transition metal carbides (MXenes). *Appl. Surf. Sci.* **2016**, *362*, 406–417. [[CrossRef](#)]
37. Wen, Y.; Li, R.; Liu, J.; Wei, Z.; Li, S.; Du, L.; Zu, K.; Li, Z.; Pan, Y.; Hu, H. A temperature-dependent phosphorus doping on $Ti_3C_2T_x$ MXene for enhanced supercapacitance. *J. Colloid Interface Sci.* **2021**, *604*, 239–247. [[CrossRef](#)]
38. Jiang, Q.; Kurra, N.; Alhabeab, M.; Gogotsi, Y.; Alshareef, H.N. All pseudocapacitive MXene-RuO₂ asymmetric supercapacitors. *Adv. Energy Mater.* **2018**, *8*, 1703043. [[CrossRef](#)]
39. Gu, T.; Wei, B. Fast and stable redox reactions of MnO₂/CNT hybrid electrodes for dynamically stretchable pseudocapacitors. *Nanoscale* **2015**, *7*, 11626–11632. [[CrossRef](#)]
40. Hu, M.; Liu, Y.; Zhang, M.; Wei, H.; Gao, Y. MnO₂/porous carbon film/Ni electrodes with high-quality interface for high rate and performance flexible supercapacitors. *Electrochim. Acta* **2016**, *218*, 58–65. [[CrossRef](#)]
41. Li, Z.; Li, H.; Song, J.; Liu, T.; He, Y.; Meng, A.; Liu, Y.; Chen, C.; Sun, C.; Hu, M.; et al. Metal-N/P coordination assisted construction of robust heterointerface for stable and superior-rate electrodes in battery-type supercapacitors. *Energy Stor. Mater.* **2022**, *50*, 252–264. [[CrossRef](#)]
42. Wang, J.; Polleux, J.; Lim, J.; Dunn, B. Pseudocapacitive contributions to electrochemical energy storage in TiO₂ (anatase) nanoparticles. *J. Phys. Chem. C* **2007**, *111*, 14925–14931. [[CrossRef](#)]
43. Wang, X.; Zhou, Y. Solid–liquid reaction synthesis of layered machinable Ti_3AlC_2 ceramic. *J. Mater. Chem.* **2002**, *12*, 455–460. [[CrossRef](#)]
44. Perdew, J.P.; Burke, K.; Ernzerhof, M. Generalized gradient approximation made simple. *Phys. Rev. Lett.* **1997**, *78*, 1396. [[CrossRef](#)]
45. Kresse, G.; Joubert, D. From ultrasoft pseudopotentials to the projector augmented-wave method. *Phys. Rev. B* **1999**, *59*, 1758–1775. [[CrossRef](#)]
46. Liao, L.; Jiang, D.; Zheng, K.; Zhang, M.; Liu, J. Industry-scale and environmentally stable $Ti_3C_2T_x$ MXene based film for flexible energy storage devices. *Adv. Func. Mater.* **2021**, *31*, 2103960. [[CrossRef](#)]

Disclaimer/Publisher’s Note: The statements, opinions and data contained in all publications are solely those of the individual author(s) and contributor(s) and not of MDPI and/or the editor(s). MDPI and/or the editor(s) disclaim responsibility for any injury to people or property resulting from any ideas, methods, instructions or products referred to in the content.